Mesopelagic respiration near the ESTOC (European Station for Time-Series in the Ocean, 15.5 °W, 29.1 °N) site inferred from a tracer conservation model

B. Fernández-Castro[1]   J. Arístegui[2]   L. Anderson[3]   M. F. Montero[2]

S. Hernández-León[2]   E. Marañón[1]   B. Mouriño-Carballido[1]

May 23, 2016

---

[1]Departamento de Ecoloxía e Bioloxía Animal, Universidade de Vigo, 36310, Vigo, Spain.

[2]Instituto de Oceanografía y Cambio Global (IOCAG), Universidad de Las Palmas de Gran Canaria, 35017, Las Palmas de Gran Canaria, Spain

[3]Applied Ocean Physics and Engineering Department, Woods Hole Oceanographic Institution, Woods Hole, MA 02543-1541, USA.

Corresponding Author: B. Fernández-Castro, Departamento de Ecoloxía e Bioloxía Animal, Universidade de Vigo, 36310, Vigo, Spain. E-mail: `bieito.fernandez@uvigo.es`

1

Abstract

Remineralization of organic matter in the mesopelagic zone (ca. 150–700 m) is a key controlling factor of carbon export to the deep ocean. By using a tracer conservation model applied to climatological data of oxygen, dissolved inorganic carbon (DIC) and nitrate, we computed mesopelagic respiration at the ESTOC (European Station for Time-Series in the Ocean, Canary Islands) site, located in the Eastern boundary region of the North Atlantic subtropical gyre. The tracer conservation model included vertical Ekman advection, geostrophic horizontal transport and vertical diffusion, and the biological remineralization terms were diagnosed by assuming steady state. Three different approaches were used to compute reference velocities used for the calculation of geostrophic velocities and flux divergences: a no-motion level at 3000 m, surface geostrophic velocities computed from the averaged absolute dynamic topography field, and surface velocities optimized from the temperature model. Mesopelagic respiration rates computed from the model were 2.8–8.9 mol O_2 m^2 y^{-1}, 2.0–3.1 mol C m^2 y^{-1} and 0.6–1.0 mol N m^2 y^{-1}, consistent with remineralization processes occurring close to Redfield stoichiometry. Model estimates were in close agreement with respiratory activity, derived from electron transport system (ETS) measurements collected in the same region at the end of the winter bloom period (3.61 ± 0.48 mol O_2 m^{-2} y^{-1}). According to ETS estimates, 50% of the respiration in the upper 1000 m took place below 150 m. Model results showed that oxygen, DIC and nitrate budgets were dominated by lateral advection, pointing to horizontal transport as the main source of organic carbon fuelling the heterotrophic respiration activity in this region.

Keywords: Mesopelagic respiration; tracer conservation model; horizontal advection; North Atlantic subtropical gyre; ESTOC

Highlights:

- Model-derived mesopelagic respiration at ESTOC is in agreement with *in vitro* estimates

- Half of the mesopelagic respiration takes place below 150 m

- Horizontal transport is the main source of organic carbon fuelling respiration

2

1 Introduction

The sunlit surface waters of the ocean are responsible for an annual photosynthetic fixation of ~50 Pg of carbon, which represents about half of the global primary production (Field et al., 1998). A fraction of the produced organic matter, ca. 5–12 Pg (Henson et al., 2011), is exported to deeper layers of the oceans where it fuels the metabolism of the heterotrophic microbial community. Part of the exported material is remineralized within the mesopelagic or 'twilight' zone (ca. 150 – 700 m), where light penetrates but is not sufficiently intense to support net photosynthesis. This zone acts as a hub between surface and deeper layers, potentially controlling the export of carbon to the deep ocean through the strength of recycling processes. Recent studies have shown that mesopelagic bacterial communities can be more active than previously thought, as they support respiration rates equivalent to those of epipelagic communities (Arístegui et al., 2009, Weinbauer et al., 2013). However, organic carbon supply estimates, accounting for both sinking particulate (POC) and dissolved organic carbon (DOC), are consistently insufficient to satisfy the estimated carbon demand of the mesopelagic communities (Arístegui et al., 2002, Burd et al., 2010). This imbalance could be compensated by other sources of organic carbon, such as non-sinking or suspended POC, which escape capture by sediment traps (Herndl and Reinthaler, 2013, Baltar et al., 2010, Alonso-González et al., 2009), and active biological flux by zooplankton (Putzeys et al., 2011, Giering et al., 2014). Moreover, the discrepancy could also be the result of methodological uncertainties in the determination of planktonic metabolic rates.

Prokaryotic respiration is a crucial term in the mesopelagic carbon budget. It is frequently derived from bacterial carbon production estimates and assumed bacterial growth efficiency, or calculated from measurements of enzymatic ETS (electron transport system) respiratory activity. Respiration estimates derived from ETS depend on the conversion factor used to transform ETS activities into oxygen consumption rates (the R:ETS ratio). Recent studies pointed out that this ratio can vary about one order of magnitude depending on the physiological state of the heterotrophic communities (Arístegui et al., 2005, Reinthaler et al., 2006). Respiration rates

3

⁵⁶ based on biogeochemical approaches, which integrate larger temporal and spatial scales and a

⁵⁷ broader array of processes, could help to reconcile the different estimates (Burd et al., 2010).

⁵⁸ Biogeochemical calculations were initially restricted to certain locations where the age of the

⁵⁹ water masses can be calculated with relative confidence (Jenkins, 1982), or where the seasonal-

⁶⁰ ity of biogeochemical tracers is large enough to infer annual averaged respiration rates (Jenkins

⁶¹ and Goldman, 1985, Martz et al., 2008). However, in regions where horizontal transport is

⁶² significant, conservation models can be used to infer respiration rates despite relatively weak

⁶³ seasonality in tracers concentrations (Fernández-Castro et al., 2012).

⁶⁴ The ESTOC (European Station for Time-Series in the Ocean, Canary Islands, 15.5°W,

⁶⁵ 29.16 ° N) site is located in the eastern boundary region of the North Atlantic subtropical gyre

⁶⁶ (NASE), and it is indirectly influenced by the coastal African upwelling, which exports nutri-

⁶⁷ ents and organic matter towards the centre of the gyre by filaments and Ekman transport (Neuer

⁶⁸ et al., 1997, Pelegrí et al., 2005, Álvarez Salgado et al., 2007). Here we adapt the 1D tracer

⁶⁹ conservation model described in Fernández-Castro et al. (2012) to quantify mesopelagic respi-

⁷⁰ ration at the ESTOC site. This estimate is compared to the averaged respiration derived from

⁷¹ ETS measurements carried out at this location in March 2000, coinciding with the end of the

⁷² late winter bloom.

⁷³ 2 Methods

⁷⁴ 2.1 Model description

A tracer conservation model was applied to temperature, oxygen, dissolved inorganic carbon

(DIC) and nitrate (NO_3) data from the ESTOC region in order to infer mesopelagic (150-700 m)

respiration. The model was adapted from Fernández-Castro et al. (2012) and includes the main

physical process which are relevant below the mixed layer: vertical diffusion, vertial advection

(Ekman transport) and horizontal advection. The temporal evolution of a tracer profile ($C =$

$C(t, z)$) –where C, t and z represent temperature or tracer concentration, time, and, vertical

⁴

coordinate, respectively– is described by the following equation:

$$\frac{\partial C}{\partial t} = -u\frac{\partial C}{\partial x} - v\frac{\partial C}{\partial y} - w\frac{\partial C}{\partial z} + K\frac{\partial^2 C}{\partial z^2} + J_C \tag{1}$$

75 where $u(z)$ and $v(z)$ are the longitudinal and latitudinal geostrophic velocities, respectively;
76 $\partial C/\partial x$ and $\partial C/\partial y$ the longitudinal and latitudinal gradients of temperature or tracer concen-
77 tration; K vertical diffusivity; w vertical velocity and $J_C(z)$ represents the sources minus sinks
78 term. For temperature J_C represents the effect of the solar shortwave radiation that penetrates
79 below the mixed layer depth, whereas for oxygen, DIC and NO_3 it represents the net effect of
80 photosynthesis and respiration computed diagnosticaly at the end of the simulation. The tem-
81 perature model was used to optimize K and the tracer models were used to infer net respiration
82 rates. The vertical domain of the model extended from the base of the mixed layer down to
83 1000 m, with a vertical resolution of 2 m.

The model was initialised with annual profiles of temperature and tracers. It was then
run for 365 days with a time step of $dt = 0.005$ days forced with annually-averaged physics
(see below). At the end of this period a new tracer profile was produced. The profile of the
biological production–consumption term was then inferred from the difference between the
initial (observed, obs.) and the final (modelled, mod.) profile under the assumption of steady
state:

$$J_C(z) = -\frac{C_{\text{obs}}(z) - C_{\text{mod}}(z)}{365\,\text{d}}\ (\text{mmol}\,\text{m}^{-3}\,\text{d}^{-1}) \tag{2}$$

84 Depth-integrated rates between 150 and 700 m are reported in the text in order to avoid bound-
85 ary effects when calculating mesopelagic respiration.

Vertical diffusivity (K) was treated as an unknown constant in our model and it was com-
puted from the optimization of the temperature (T) model run. The optimal K was estimated
by minimizing the following cost function:

$$\text{Cost} = \left(\frac{1}{550\,\text{m}} \int_{150\,\text{m}}^{700\,\text{m}} \left(\frac{T_{\text{obs}}(z) - T_{\text{mod}}(z)}{\max(T_{\text{obs}}(z)) - \min(T_{\text{obs}}(z))}\right)^2 dz\right)^{1/2} \tag{3}$$

5

Averaged annual temperature, oxygen and NO_3 profiles were derived from the World Ocean Atlas 2009 (WOA09, Locarnini et al. (2010), Garcia et al. (2010b,a)) and computed as the mean profile of the four grid points nearest to the ESTOC site (see Figure 1). The DIC profile was calculated in a similar way using data from the Global Data Analysis Project (GLODAP) climatology (Key et al., 2004). The standard deviation was used as the error estimate.

Monthly solar shortwave radiation for the period 1996-2001 from the CORE.2 Global Air-Sea flux dataset (`http://rda.ucar.edu/datasets/ds260.2/`) was used to calculate the annual mean insolation at the ESTOC site ($191.1 \pm 4.8\,\mathrm{W\,m^{-2}}$), by fitting the seasonal cycle to an harmonic function. The effect of the solar shortwave radiation that penetrates below the mixed layer (J_C term for the temperature model) was computed as:

$$J_C^T(z) = \frac{1}{\rho(z)C_p(z)}\frac{\partial I(z)}{\partial z} \tag{4}$$

where ρ is the water density computed from temperature and salinity profiles using the Millero and Poisson (1981) formulation, C_p is the specific heat (Fofonoff and Millard, 1983), and $I(z)$ is the shortwave radiation flux computed by using the attenuation model of Paulson and Simpson (1977) for Type I water and the surface shortwave radiation value.

Ekman downwelling/upwelling velocity, w, was computed from the wind stress monthly climatological data included in the International Comprehensive Ocean-Atmosphere Data Set (Leetmaa and Bunker, 1978), with a spatial resolution of $2° \times 2°$, and then annually averaged. The ESTOC site is characterized by a weak downwelling with a mean annual velocity of $-3.8 \pm 15.0\,\mathrm{m\,y^{-1}}$. The Ekman velocity was set to zero at the surface and increased linearly to the Ekman depth, considered as 30 m, and decreased linearly to zero down to 250 m (Ono et al., 2001). As depth-dependent w requires horizontal convergence or divergence for volume conservation, horizontal advection included a correction term. This was accomplished numerically by implicitly evaluating $w\partial C/\partial z$ at the grid box interfaces.

Horizontal gradients of temperature, oxygen and NO_3 were calculated using the four grid points surrounding ESTOC from the WOA09 climatology, whereas the GLODAP database was

used for DIC. Longitudinal gradients were computed as the difference between the temperature and tracer concentration averages at the B,D and A,C locations for each depth divided by the averaged distance: $(\partial C/\partial x)(z) = (\overline{C_{B,D}(z)} - \overline{C_{A,C}(z)})/dx$ (see Figure 1). Similarly, latitudinal gradients were calculated as the difference between the averages at the A,B and the C,D locations: $(\partial C/\partial y)(z) = (\overline{C_{A,B}(z)} - \overline{C_{C,D}(z)})/dy$. The standard deviations associated with each average were propagated in order to compute gradient uncertainties.

Horizontal velocities, u and v, were assumed to be geostrophic and computed from the thermal wind equations using the neutral density profiles derived from temperature and salinity WOA09 fields according to Jackett and McDougall (1997). Standard deviations in the density field were propagated in order to evaluate velocity errors. To evaluate the uncertainty due to the choice of reference level, three different reference velocities were used for the integration of the thermal wind equations. First, no-motion was assumed at 3000 m in accord with other studies in the North Atlantic (Siegel and Deuser, 1997, Alonso-González et al., 2009). Second, geostrophic surface currents derived from the averaged field of 15 years (1996-2010) Absolute Dynamic Topography (ADT) data provided by AVISO (`http://www.aviso.altimetry.fr`) were used as the reference for the integration. As spatial resolution of the AVISO database (1/4°) is higher compared to the WOA09 database (1°), surface geostrophic velocity vectors were averaged inside the model box (A,B,C,D in Figure 1). Finally, the optimal surface reference velocities (u_s, v_s) were also diagnosed from the temperature model by minimizing the cost function in equation 3.

Deviations from the steady state in the temperature model, i.e. differences between the observed and the modelled temperature profile at the end of the simulations, can occur due to inaccuracy or oversimplification of the modelled physical processes. These limitations can possibly affect the determination of the biological rates for the different tracers (C). We evaluate the detection limit for the biological rates by rescaling the change in the temperature profile due to unaccounted physical processes as:

$$J_C^{\text{Det. Lim.}}(z) = \frac{1}{365\,\text{d}} \frac{|T_{obs}(z) - T_{mod}(z)|}{\max(T_{obs}(z)) - \min(T_{obs}(z))} \times (\max(C_{obs}(z)) - \min(C_{obs}(z))), \;\; (\text{mmol m}^{-3}\,\text{d}^{-1})$$

(5)

Tracer concentration changes lower than $J_C^{\text{Det. Lim.}}$ are likely due to model inaccuracy and can not be attributed to biological uptake or production.

Furthermore, in order to determine the standard deviation of the model terms and depth-integrated rates, 2000 Monte Carlo simulations were performed for each model run with model variables randomly generated by assuming normal distributions. For the tracers, tracers gradient and velocity profiles, and other variables obtained from databases (solar radiation, w), the calculated standard deviation was used to generate random inputs. For the optimized K and surface velocities (u_s, v_s), uncertainties corresponding to 50% and 0.2 cm s^{-1} were assumed, respectively.

2.2 Electron transport system respiratory activity

Water samples for the determination of ETS respiratory activity were collected at 15 depths, from the surface down to 1000 m, during 9 samplings conducted between 12th and 23rd March 2000. Depending on depth, 5 to 20 l of seawater were pre-filtered through a 200 μm mesh and poured into acid-cleaned plastic carboys, before being filtered through 47 mm Whatman GF/F filters, at a low vacuum pressure (<1/3 atm). The filters were immediately stored in liquid nitrogen until assayed in the laboratory (within a 2-3 weeks). ETS determinations were carried out according to the Kenner and Ahmed (1975) modification of the tetrazolium reduction technique proposed by Packard (1971) as described in Arístegui and Montero (1995). An incubation time of 15 min at 18 °C was used. ETS activities measured at 18 °C were converted to respiratory activities at in situ temperatures by using the Arrhenius equation. A mean activation energy of 16 kcal mol^{-1} was used (Arístegui and Montero, 1995).

3 Results

3.1 Implementation of the tracer conservation model

Figure 2 and Table 1 show the geostrophic velocities and flux divergence for temperature, oxygen, DIC and NO$_3$ computed by using three different reference velocities: a no-motion level at 3000 m, surface geostrophic velocities computed from the averaged ADT field, and surface velocities optimized from the temperature model (see Methods). The results obtained by using the three different approaches are described in the following sections.

3.1.1 No-motion level at 3000 m

The geostrophic flow calculated by integrating the thermal wind equations considering a no-motion level at 3000 m was directed southwards from the surface ($v_s = -2.67 \pm 0.37$ cm s^{-1}, Table 1) down to 1000 m (Figure 2). The longitudinal component was insignificant at the surface ($u_s = 0.03 \pm 0.52$ cm s^{-1}) and directed westward at greater depths. The heat flux divergence indicated a net cooling of the water column by advection. The longitudinal component of the heat flux divergence ($-u\frac{\partial T}{\partial x}$) was negative throughout the water column, whereas the latitudinal component ($-v\frac{\partial T}{\partial y}$) was negative in the upper 200 m and close to zero at greater depths. Both components contributed to the depth-integrated (150–700 m) net cooling, which was -203 ± 66 °C m y^{-1} (Table 1). The latitudinal oxygen flow divergence showed positive values (convergence) from the surface down to 800 m, whereas the longitudinal component was negative throughout the water column, resulting in a net oxygen gain of 1.97 ± 3.17 mol O$_2$ m^{-2} y^{-1}. The opposite pattern was observed for DIC and NO$_3$, resulting in a net loss of both tracers (-1.22 ± 1.21 mol C m^{-2} y^{-1} and -0.35 ± 0.52 mol N m^{-2} y^{-1}). However, differences in the vertical distribution of the flow divergences were observed. Whereas DIC loss was maximum at the surface and decreased with depth (similar to the oxygen gain), NO$_3$ divergence was negative, mainly between 200 and 800 m.

The tracer conservation model was first run for temperature in order to diagnose vertical diffusivity (K). The computed optimal value was 3.9 cm^2 s^{-1} (Table 2), 5-10 fold higher com-

9

pared to diffusivity values obtained in the area by tracer release experiments (Schmitt et al., 2005) and microstructure observations (Fernández-Castro et al., 2014). There was a good agreement between the observed and the modelled temperature profiles (Figure 3), the cost function being 1.8% (see Methods). The advective (horizontal + vertical) and diffusive terms dominated the temperature budget, and the optimization of K maximises diffusivity because the cooling caused by geostrophic advection divergence was compensated by diffusion in order to minimise the net change at the end of the simulation.

The oxygen model showed an accumulation of oxygen from the initial to the final profile. In order to maintain the steady state, this accumulation was compensated by biological uptake. The J_{O_2} term showed net oxygen consumption from 100 m down to 1000 m, as the result of positive advection divergence down to 600 m, and the positive diffusion divergence below this depth. The DIC and NO_3 simulations resulted in losses of both tracers. This was mainly driven by advection in the upper 600 m and by diffusion below, and it was balanced by respiration processes. The respiration signal was also vertically decoupled for both tracers, as NO_3 respiration maximum was located deeper due to differences in the advective flux divergence. Depth-integrated respiration rates were $-2.72 \pm 3.90 \, \mathrm{mol\,O_2\,m^{-2}\,y^{-1}}$, $2.46 \pm 1.62 \, \mathrm{mol\,C\,m^{-2}\,y^{-1}}$ and $0.54 \pm 0.64 \mathrm{mol\,N\,m^{-2}\,y^{-1}}$ for oxygen, DIC and NO_3, respectively (Table 2). Despite the high uncertainty associated to these figures, the computed rates were about 5-10 fold higher than the detection limit computed from the temperature model runs (see Methods and Table 2). The respiration stoichiometry ratios were O_2:C = 1.1 ± 1.7, O_2:N = 5.0 ± 9.4 and C:N = 4.6 ± 6.2, largely consistent with respiration rates close to Redfield proportions (O_2:C = 1.4, O_2:N =9.2, C:N = 6.6). For this model configuration, the geostrophic horizontal transport dominated the tracer budgets, being responsible for 72%, 49% and 65% of the respiration rate diagnosed for oxygen, DIC and NO_3, respectively. Note that the horizontal advection term in Table 2 does not correspond directly to geostrophic advection, as it includes any divergence required to ensure mass conservation (see Methods). Vertical diffusion accounted for 27%, 52% and 37%, respectively, whereas the contribution of the Ekman transport (vertical advection) was very low.

3.1.2 Surface velocities derived from absolute dynamic topography

The surface geostrophic flow calculated from the averaged ADT field had a similar southwards component ($v_s = -2.39 \pm 0.78$ cm s^{-1}) compared to that obtained from the reference no-motion level at 3000 m (Table 1). However, in this case a significant eastward component ($u_s = 1.11 \pm 0.66$ cm s^{-1}) was also computed. The eastward flow was caused by the contribution of velocity vectors computed in the northern part of the model box (see Figure 1). The geostrophic flow was also directed southeastwards at deeper levels (Figure 2), resulting in positive heat flux divergence (net heating, $233 \pm 67\,^\circ$C m y^{-1}), mainly driven by the longitudinal component. Contrary to the previous approach, oxygen convergence and DIC and NO$_3$ divergences were enhanced by the eastward component, which resulted in higher depth-integrated respiration rates (8.71 ± 2.81 mol O$_2$ m^2 y^{-1}, -2.92 ± 1.22 mol C m^2 y^{-1} and -1.04 ± 0.49 mol N m^2 y^{-1}). The optimal K value diagnosed from the temperature model was 0.4 cm^{2}s^{-1} (Table 2), in better agreement with the observations. However, the temperature model cost function was 3.0%, slightly higher than in the previous configuration. The temperature and oxygen (DIC and NO$_3$) profiles showed accumulation (loss) at the end of the simulations (Figure 4). Due to the lower diffusivity, advection was the most important driver for these patterns. Depth-integrated respiration rates were -8.86 ± 3.93 mol O$_2$ m^{-2} y^{-1}, 3.09 ± 1.63 mol C m^{-2} y^{-1} and 1.07 ± 0.68 mol N m^{-2} y^{-1}. These values were higher compared to the previous approach, although the model uncertainty was also larger as illustrated by the higher detection limits (Table 2). The respiration stoichiometry ratios were O$_2$:C $= 2.9 \pm 2.0$, O$_2$:N $= 8.3 \pm 6.4$ and C:N $= 2.9 \pm 2.4$. In this case the relative contribution of the geostrophic transport to the diagnosed respiration rates was more important, reaching $> 95\%$ for all the tracers. Together, vertical diffusion and advection, represented $< 5\%$ of the tracers budget.

3.1.3 Surface velocities optimized from the temperature model

Due to the sensitivity of our model to the geostrophic transport and, in turn, to the used reference velocities, we performed a triple optimization process for diffusivity (K) and surface

11

²³³ reference velocities (u_s, v_s). During this process, the temperature model cost function was
²³⁴ evaluated for a set of plausible K, u_s and v_s values (Figure 5). The diagnosed optimal param-
²³⁵ eters were $K = 1\,\mathrm{cm^2\,s^{-1}}$, $u_s = 0.4\,\mathrm{cm\,s^{-1}}$ and $v_s = -2.4\,\mathrm{cm\,s^{-1}}$. Optimal diffusivity values
²³⁶ lower than $1\,\mathrm{cm^2\,s^{-1}}$, in good agreement with the observations, were only possible for eastward
²³⁷ (positive) velocities lower than the value of $u_s = 1.11\,\mathrm{cm\,s^{-1}}$ computed from the ADT field.
²³⁸ Lower cost values were also computed for close to zero or negative u_s, but in this case optimal
²³⁹ diffusivity was unrealistically high, and therefore these possibilities were discarded.

²⁴⁰ The latitudinal component of the geostrophic transport was also southwards in the upper
²⁴¹ 600 m, due to similar surface values in comparison to the previous approaches (Figure 2). The
²⁴² longitudinal component was westwards, except at the surface and below 700 m, and velocity
²⁴³ values were lower compared to the previous approaches. The net heat flux divergence was neg-
²⁴⁴ ative through the water column, and the depth-integrated net change ($-73 \pm 57\,\mathrm{°C\,m\,y^{-1}}$) was
²⁴⁵ smaller compared to the first approach (no-motion level at 3000 m). The net flux divergences
²⁴⁶ for oxygen, DIC and NO_3 showed a similar pattern compared to the first approach, because in
²⁴⁷ this case both longitudinal and latitudinal flux divergences were reduced.

²⁴⁸ Despite the lower diffusivity, initial and final temperature profiles were in close agreement
²⁴⁹ in this simulation, with a computed cost of 1.6% (Figure 6 and Table 2). Temperature changes
²⁵⁰ due to horizontal advection were smaller compared to the other two approaches, because the
²⁵¹ optimization process reduced the heat advection flux divergence, instead of maximising the
²⁵² compensatory diffusion. This was mainly accomplished by the optimization of the longitudinal
²⁵³ component of the flow, which was mainly responsible for the heat divergence. The model
²⁵⁴ results for oxygen, DIC and NO_3 were very similar to those from the first approach, although
²⁵⁵ small differences were noticed in the vertical distribution of the biological term, due to the
²⁵⁶ different interplay of diffusive and advective processes. Depth-integrated respiration rates were
²⁵⁷ $-4.39 \pm 7.02\,\mathrm{mol\,O_2\,m^{-2}\,y^{-1}}$, $2.00 \pm 2.63\,\mathrm{mol\,C\,m^{-2}\,y^{-1}}$ and $0.57 \pm 1.05\,\mathrm{mol\,N\,m^{-2}\,y^{-1}}$, very
²⁵⁸ similar to the first approach, whereas the stoichiometric ratios were O_2:C = 2.2 ± 4.5, O_2:N =
²⁵⁹ 7.7 ± 18.8 and C:N = 3.5. In this case, the geostrophic transport flux divergence represented
²⁶⁰ $50 - 60\%$ of the computed respiration.

12

²⁶¹ Due to the good agreement between the results derived from this approach and the no-
²⁶² motion level at 3000 m, the realistic optimized K value, and the lower detection limits, we
²⁶³ decided to use the mesopelagic respiration rates computed with this configuration for compar-
²⁶⁴ ison with estimates derived from ETS observations.

²⁶⁵ 3.2   Mesopelagic respiration derived from ETS respiratory activity

²⁶⁶ The vertical distribution of averaged respiration rates derived from ETS measurements carried
²⁶⁷ out at the ESTOC site from 12th to 23rd March 2000 is shown in Figure 7. ETS respiration rates
²⁶⁸ were higher above 100 m (ca. 0.1 mmol O_2 m^{-3} d^{-1}) and progressively decreased down to 200
²⁶⁹ m (ca. 0.05 mmol O_2 m^{-3} d^{-1}). Below this depth, respiration rates showed small vertical vari-
²⁷⁰ ability ranging between 0.007 and 0.016 mmol O_2 m^{-3} d^{-1}. The averaged depth-integrated (20–
²⁷¹ 1000 m) respiration rate was 8.57 ± 0.76 mol O_2 m^{-2} y^{-1} (23.5 ± 2.1 mmol O_2 m^{-2} d^{-1}), 50% of
²⁷² the total rate (4.50 ± 0.52 mol O_2 m^{-2} y^{-1}) occurring between 150 and 1000 m.

²⁷³ The vertical distribution of ETS mesopelagic respiration was in close agreeement with the
²⁷⁴ biological terms derived for oxygen and DIC from the tracer conservation model, especially
²⁷⁵ between 150 and 700 m. Modelled respiration for NO_3, subjected to larger uncertainty, showed
²⁷⁶ a deeper maximum at around 400 m. Note that the upper limit for the model configuration
²⁷⁷ was the mixed layer depth, and that the region above 150 m is likely affected by bound-
²⁷⁸ ary effects, because the concentration is forced to climatological values in this layer where
²⁷⁹ air-sea gas exchange is not considered. Depth-integrated (150–700 m) ETS respiration was
²⁸⁰ 3.61 ± 0.48 mol O_2 m^{-2} y^{-1} (2.56 ± 0.34mol C m^{-2} y^{-1} and 0.388 ± 0.052 mol N m^{-2} y^{-1}, us-
²⁸¹ ing Redfield stoichiometry for the conversion), in close agreement with model estimates for
²⁸² oxygen (2.8–8.9 mol O_2 m^2 y^{-1}) and DIC (2.0–3.1 mol C m^2 y^{-1}), and slightly lower for NO_3
²⁸³ (0.56–1.07mol N m^{-2} y^{-1}) (Table 2).

4 Discussion

4.1 Comparison of mesopelagic respiration inferred from the tracer conservation model and ETS measurements

Respiration estimates derived from the tracer conservation model and ETS measurements account for distinct processes occurring at different temporal and spatial scales. ETS measurements were carried out near the ESTOC site during the late winter bloom, which constitutes the most productive season in the region (Neuer et al., 2007), whereas the tracer conservation model integrates larger temporal and spatial scales implicit in the climatologies. Furthermore, whereas ETS measurements account for the potential respiration of the $< 200\,\mu m$ size-fraction microbial plankton (see Methods), the model quantifies total respiration processes relevant on annual time-scales. The comparison of the ETS measurements reported here with ETS respiration of the larger size-fraction ($> 200\,\mu m$), quantified for the same cruise, ($0.52 \pm 0.15\,mol\,O_2\,m^{-2}\,y^{-1}$, Putzeys et al., 2011), indicates that the smaller size organisms dominate ($\approx 87\%$) mesopelagic respiration. Despite the mentioned limitations, mesopelagic respiration derived from the tracer conservation model for the three tracers was in close agreement with ETS respiration estimated in the same region in March 2000 ($3.61 \pm 0.48\,mol\,O_2\,m^{-2}\,y^{-1}$, or $4.13 \pm 0.50\,mol\,O_2\,m^{-2}\,y^{-1}$ both size-fractions included), when a R:ETS = 0.086, representative for low bacterial activity, (Packard et al., 1988) was used.

A previous estimate of global respiration in the dark ocean (below 200 m depth) ($5\,mol\,C\,m^{-2}\,y^{-1}$, Arístegui et al., 2003a), derived by up-scaling ETS measurements using the same R:ETS ratio, was also in good agreement with several estimates based on geochemical tracers (Jenkins, 1982, Jenkins and Wallace, 1992, Carlson et al., 1994). However, an R:ETS ratio of 0.68 ± 0.11 was inferred from the comparison of oxygen consumption estimates and ETS measurements carried out in the mesopelagic south of the Canary Islands, leading to an estimate of mesopelagic respiration of $68 \pm 8\,mmol\,C\,m^{-2}\,d^{-1}$ ($24.8 \pm 2.9\,mol\,C\,m^{-2}\,y^{-1}$) (Arístegui et al., 2005), one order of magnitude higher than the values reported here. The region south of the Canary Islands is generally more productive (Arístegui et al., 1997), compared to the northern region, due to

14

the nearby upwelling system and also to the intense mesoscale activity generated downstream of the islands (Arístegui et al., 1994, Sangrà et al., 2009). For this reason, the measurements reported by Arístegui et al. (2005) probably describe a relatively fast-growing heterotrophic community as a result of the enhanced phytoplankton productivity that generally characterizes this region. The good agreement between ETS and model derived respiration, despite the different temporal and spatial scales implicit in both estimates, suggest that the seasonal variability of mesopelagic remineralization processes in this region is relatively weak. This is consistent with previous studies reporting a small seasonal variability in POC sinking fluxes (Helmke et al., 2010) and suspended POC concentrations (Neuer et al., 2007) at the ESTOC site.

4.2 The mesopelagic carbon budget in the eastern and western subtropical North Atlantic

Mesopelagic respiration rates reported in this study were in close agreement with geochemical estimates, based on ^{3}He/^{3}H water masses age and apparent oxygen utilisation (AOU) determinations, carried out below 100 m in the beta triangle region, located west of the ESTOC site ($5.7\,\mathrm{mol\,O_2\,m^{-2}\,y^{-1}}$, Jenkins, 1982). Our estimates were also very similar to the value reported for the Sargasso Sea, in the subtropical Northwestern Atlantic (NASW), by using the seasonal variation of oxygen concentration below 100 m (4.1–$5.9\,\mathrm{mol\,O_2\,m^{-2}\,y^{-1}}$, Jenkins and Goldman, 1985). Despite the similarities between mesopelagic respiration reported for the eastern and western subtropical North Atlantic, the two regions are characterized by important differences regarding the sources of the organic carbon fuelling remineralization processes in the mesopelagic zone.

Our model results indicate that oxygen, DIC and NO$_3$ budgets at ESTOC were mainly dominated by lateral processes, due to the southward transport along the Canary Current. We are aware that these results are sensitive to the calculation of geostrophic flux divergences, which were derived from global climatologies, and for this reason subjected to important uncertainties (see Methods and Table 2). However, our results were consistent when different approaches were used to determine the reference velocities used for the calculation of geostrophic trans-

15

ports (Table 2). In agreement with previous studies (Arístegui et al., 2003b, Álvarez Salgado et al., 2007, Alonso-González et al., 2009), our results point out to the horizontal transport as the main source of organic carbon for the mesopelagic respiratory activity in this region.

Vertical fluxes of sinking particulate organic carbon determined by surface-tethered sediment traps deployed at 200 m at ESTOC, covering seasonality during three years, ranged between 0.097 and 0.173 mol C m^{-2} y^{-1}) (Helmke et al., 2010), which is about one order of magnitude lower compared to our estimates of mesopelagic respiration (2.00–3.09 mol C m^{-2} y^{-1}) (Figure 8). By using a box model approach, Alonso-González et al. (2009) estimated the lateral transport and consumption of suspended particulate organic carbon, between 100 and 700 m, in the southern Canary Current region away from the influence of the eddy field. According to these authors, the organic carbon supply by this process was 0.52 mol C m^{-2} y^{-1}. Moreover, by comparing the AOU and DOC distributions, Arístegui et al. (2003b) calculated that DOC transported from the coastal African upwelling account for 27% of the mesopelagic respiration in this region. By extrapolating this result to our data, we estimated a contribution of DOC ranging between 0.54 and 0.81 mol C m^{-2} y^{-1}. Putzeys et al. (2011) calculated the active flux mediated by diel migrant zooplankton to be 0.053–0.15 mol C m^{-2} y^{-1} close to the ESTOC site. The sum of all these processes (1.2–1.7 mol C m^{-2} y^{-1}), which was in good agreement with the mass balance reported by Alonso-González et al. (2009) (0.88–1.87 mol C m^{-2} y^{-1}), accounts for $38 - 83\%$ of the diagnosed respiration for the ESTOC site (Figure 8). These results highlight the lateral supply of DOC and suspended POC as the two major contributors to the mesopelagic carbon budget in this region, whereas vertical passive and active fluxes only account for less than 20% of the carbon demand.

In NASW, which is located further from productive areas, seasonal ventilation is considered the main source for oxygen in the mesopelagic zone (Jenkins and Goldman, 1985). Vertical fluxes of sinking particulate organic carbon determined by sediment traps at BATS (Bermuda Atlantic Time-Series Study, 31.7°N-64.2°W) are 3-4 fold higher than the values reported for ESTOC (0.3–0.8 mol C m^{-2} y^{-1}, Neuer et al., 2002, Helmke et al., 2010, Owens et al., 2013) (Figure 8). At BATS, the vertical export of dissolved organic carbon due to entrainment into

16

the thermocline during winter mixing has been estimated to be 0.99–1.21 mol C m^{-2} y^{-1} (Carlson et al., 1994). More recently, Emerson (2014) estimated as 13% the contribution of DOC to the variation in AOU below 100 m. Considering the value of total mesopelagic respiration estimated by Jenkins and Goldman (1985) (4.1–5.9 mol O$_2$ m^{-2} y^{-1}), we computed the contribution of DOC to total respiration as 0.38–0.54 mol C m^{-2} y^{-1}, slightly lower than the previous estimate by Carlson et al. (1994). On the other hand, the active carbon flux by migrating zooplankton in this region has been quantified as 0.06 mol C m^{-2} y^{-1} (Steinberg et al., 2000). The sum of all these fluxes (0.74–2.07 mol C m^{-2} y^{-1}) accounts for $18 - 70\%$ of the organic carbon demand between 100 and 800 m (2.93–4.21 mol C m^{-2} y^{-1}, Jenkins and Goldman, 1985) (Figure 8). The lack of agreement between carbon sources and sinks in the BATS region has been attributed to inefficient performance of sediment traps (Buesseler et al., 2007), intense shallow remineralization between the euphotic depth (ca. 100 m) and the depth of the shallower trap (150 m), and also to the carbon supply through lateral processes (Emerson, 2014). Although, as far as we know, the lateral transport of organic carbon at this site has not been evaluated so far, its contribution to the mesopelagic carbon budget is probably lower compared to ESTOC. This argument is supported by the comparison of vertical profiles of POC collected at both sites (Figure 9). Whereas the fluxes of sinking particulate organic carbon are much lower at ESTOC, depth-integrated (150–700 m) averaged POC concentration at this site (2.65 mol m^{-2}, Neuer et al., 2007) is about 6-fold higher compared to BATS (0.41 mol m^{-2}), which may reflect the accumulation of slow-sinking suspended particles exported from the adjacent, coastal upwelling region.

Recent studies argue against the common assumption that oligotrophic subtropical regions are relatively homogeneous regarding the contribution of the marine biota to the ocean carbon cycle (Mouriño-Carballido and Neuer, 2008, Neuer et al., 2002). In support of this, our results highlight the importance of regional variability in the contribution of different processes of organic matter transport and cycling in the mesopelagic zone in these regions. Together with synthesis and remineralization of organic matter in shallow waters, respiratory activity in the mesopelagic controls the amount of carbon to be exported from the sunlit surface waters to the

17

deep ocean (Kwon et al., 2009). Quantifying its magnitude, but also understanding geograph-ical differences in the relevance of the vertical and horizontal processes involved in the supply of organic carbon in this layer, is crucial to determine the role of the open-ocean marine biota in the global carbon cycle.

Acknowledgements

References

Alonso-González, I. J., Arístegui, J., Vilas, J. C., and Hernández-Guerra, A. (2009). Lateral POC transport and consumption in surface and deep waters of the Canary Current region: A box model study. *Global Biogeochem. Cycles*, 23(2):GB2007.

Álvarez Salgado, X. A., Arístegui, J., Barton, E. D., and Hansell, D. A. (2007). Contribution of upwelling filaments to offshore carbon export in the subtropical Northeast Atlantic Ocean. *Limnol. Oceanogr.*, 52(3):1287–1292.

Arístegui, J., Agustí, S., and Duarte, C. M. (2003a). Respiration in the dark ocean. *Geophys. Res. Lett.*, 30(2):1–4.

Arístegui, J., Barton, E. D., Montero, M. F., Garcia-Muñoz, M., and Escánez, J. (2003b). Organic carbon distribution and water column respiration in the NW Africa-Canaries Coastal Transition Zone. *Aquat. Microb. Ecol.*, 33:289–301.

Arístegui, J., Duarte, C. M., Agustí, S., Doval, M., Alvarez-Salgado, X. a., and Hansell,

D. a. (2002). Dissolved organic carbon support of respiration in the dark ocean. *Science*, 298:1967.

Arístegui, J., Duarte, C. M., Gasol, J. M., and Alonso-Sáez, L. (2005). Active mesopelagic prokaryotes support high respiration in the subtropical northeast Atlantic Ocean. *Geophys. Res. Lett.*, 32:1–4.

Arístegui, J., Gasol, J. M., Duarte, C. M., and Herndl, G. J. (2009). Microbial oceanography of the dark ocean's pelagic realm. *Limnol. Oceanogr.*, 54(5):1501–1529.

Arístegui, J. and Montero, M. F. (1995). The relationship between community respiration and ETS activity in the ocean. *J. Plankton Res.*, 17(7):1563–1571.

Arístegui, J., Sangrá, P., Hernández-León, S., Cantón, M., Hernández-Guerra, A., and Kerling, J. (1994). Island-induced eddies in the Canary islands. *Deep Sea Res. I*, 41(10):1509–1525.

Arístegui, J., Tett, P., Hernández-Guerra, A., Basterretxea, G., Montero, M. F., Wild, K., Sangrá, P., Hernández-Leon, S., Canton, M., García-Braun, J., Pacheco, M., and Barton, E. (1997). The influence of island-generated eddies on chlorophyll distribution: a study of mesoscale variation around Gran Canaria. *Deep Sea Res. Part I Oceanogr. Res. Pap.*, 44(1):71–96.

Baltar, F., Arístegui, J., Sintes, E., Gasol, J. M., Reinthaler, T., and Herndl, G. J. (2010). Significance of non-sinking particulate organic carbon and dark CO 2 fixation to heterotrophic carbon demand in the mesopelagic northeast Atlantic. *Geophys. Res. Lett.*, 37(9):L09602.

Buesseler, K. O., Lamborg, C. H., Boyd, P. W., Lam, P. J., Trull, T. W., Bidigare, R. R., Bishop, J. K. B., Casciotti, K. L., Dehairs, F., Elskens, M., Honda, M., Karl, D. M., Siegel, D. A., Silver, M. W., Steinberg, D. K., Valdes, J., Van Mooy, B., and Wilson, S. (2007). Revisiting carbon flux through the ocean's twilight zone. *Science*, 316(5824):567–570.

Burd, A. B., Hansell, D. A., Steinberg, D. K., Anderson, T. R., Arístegui, J., Baltar, F., Beaupre, S. R., Buesseler, K. O., Dehairs, F., Jackson, G. A., Kadko, D. C., Koppelmann, R., Lampitt,

R. S., Nagata, T., Reinthaler, T., Robinson, C., Robison, B. H., Tamburini, C., and Tanaka, T. (2010). Assessing the apparent imbalance between geochemical and biochemical indicators of meso- and bathypelagic biological activity: What the @$]!is wrong with present calculations of carbon budgets? *Deep Sea Res. II*, 57:1557–1571.

Carlson, C., Ducklow, H., and Michaels, A. (1994). Annual flux of dissolved organic carbon from the euphotic zone in the northwestern Sargasso Sea. *Nature*, 371:405–408.

Emerson, S. (2014). Annual net community production and the biological carbon flux in the ocean. *Global Biogeochem. Cycles*, 28:14–28.

Fernández-Castro, B., Anderson, L., Marañón, E., Neuer, S., Ausín, B., Gonzáez-Dávila, M., Santana-Casiano, J. M., Cianca, A., Santana, R., Llinás, O., Rueda, M. J., and Mouriño Carballido, B. (2012). Regional differences in modelled net production and shallow remineralization in the North Atlantic subtropical gyre. *Biogeosciences*, 9(8):2831–2846.

Fernández-Castro, B., Mouriño Carballido, B., Benítez-Barrios, V., Chouciño, P., Fraile-Nuez, E., Graña, R., Piedeleu, M., and Rodríguez-Santana, A. (2014). Microstructure turbulence and diffusivity parameterization in the tropical and subtropical Atlantic, Pacific and Indian Oceans during the Malaspina 2010 expedition. *Deep Sea Res. I*, 94:15–30.

Field, C. B., Behrenfeld, M. J., Randerson, J. T., and Falkowski, P. (1998). Primary production of the biosphere: Integrating terrestrial and oceanic components. *Science*, 281(5374):237–240.

Fofonoff, N. P. and Millard, R. C. (1983). Algorithms for computation of fundamental properties of seawater. *Unesco Technical Papers in Marine Science*, 44:53.

Garcia, H. E., Locarnini, R. A., Boyer, T., Antonov, J. I., Zweng, M., and Johnson, D. R. (2010a). *World Ocean Atlas 2009, Volume 3: Dissolved Oxygen, Apparent Oxygen Utilization, and Oxygen Saturation.* NOAA Atlas NESDIS 70, U.S. Government Printing Office, Washington, D.C.

Garcia, H. E., Locarnini, R. A., Boyer, T., Antonov, J. I., Zweng, M., and Johnson, D. R. (2010b). *World Ocean Atlas 2009, Volume 4: Nutrients (phosphate, nitrate, silicate)*. NOAA Atlas NESDIS 71, U.S. Government Printing Office, Washington, D.C.

Giering, S. L. C., Sanders, R., Lampitt, R. S., Anderson, T. R., Tamburini, C., Boutrif, M., Zubkov, M. V., Marsay, C. M., Henson, S. a., Saw, K., Cook, K., and Mayor, D. J. (2014). Reconciliation of the carbon budget in the ocean's twilight zone. *Nature*, 507(7493):480–3.

Helmke, P., Neuer, S., Lomas, M. W., Conte, M., and Freudenthal, T. (2010). Cross-basin differences in particulate organic carbon export and flux attenuation in the subtropical North Atlantic gyre. *Deep Sea Res. I*, 57(2):213–227.

Henson, S. A., Sanders, R., Madsen, E., Morris, P. J., Le Moigne, F., and Quartly, G. D. (2011). A reduced estimate of the strength of the ocean's biological carbon pump. *Geophys. Res. Lett.*, 38(4):10–14.

Herndl, G. J. and Reinthaler, T. (2013). Microbial control of the dark end of the biological pump. *Nat. Geosci.*, 6(9):718–724.

Jackett, D. R. and McDougall, T. J. (1997). A Neutral Density Variable for the World's Oceans. *J. Phys. Oceanogr.*, 27(2):237–263.

Jenkins, W. J. (1982). Oxygen utilization rates in North Atlantic subtropical gyre and primary production in oligotrophic systems. *Nature*, 300(5889):246–248.

Jenkins, W. J. and Goldman, J. C. (1985). Seasonal oxygen cycling and primary production in the Sargasso Sea. *J. Mar. Res.*, 43(2):465–491.

Jenkins, W. J. and Wallace, D. W. R. (1992). Tracer Based Inferences of New Primary Production in the Sea. In Falkowski, P., Woodhead, A., and Vivirito, K., editors, *Prim. Product. Biogeochem. Cycles Sea*, volume 43 of *Environmental Science Research*, pages 299–316. Springer US.

Kenner, R. A. and Ahmed, S. I. (1975). Measurements of electron transport activities in marine phytoplankton. *Mar. Biol.*, 33(2):119–127.

Key, R. M., Kozyr, A., Sabine, C. L., Lee, K., Wanninkhof, R., Bullister, J. L., Feely, R. A., Millero, F. J., Mordy, C., and Peng, T. H. (2004). A global ocean carbon climatology: Results from Global Data Analysis Project (GLODAP). *Global Biogeochem. Cycles*, 18(4):1–23.

Kwon, E. Y., Primeau, F., and Sarmiento, J. L. (2009). The impact of remineralization depth on the air–sea carbon balance. *Nat. Geosci.*, 2(9):630–635.

Leetmaa, A. and Bunker, A. F. (1978). Updated charts of the mean annual wind stress, convergences in Ekman Layers, and Sverdrup transport in the North Atlantic. *J. Mar. Res.*, 36:311–322.

Locarnini, R. A., Mishonov, A. V., Antonov, J. I., Boyer, T. P., Garcia, H. E., Baranova, O. K., Zweng, M. M., and Johnson, D. R. (2010). *World Ocean Atlas 2009, Volume 1: Temperature.* NOAA Atlas NESDIS 71, U.S. Government Printing Office, Washington, D.C.

Martz, T. R., Johnson, K. S., and Riser, S. C. (2008). Ocean metabolism observed with oxygen sensors on profiling floats in the South Pacific. *Limnol. Oceanogr.*, 53(5, part 2):2094–2111.

Millero, F. J. and Poisson, A. (1981). International one-atmosphere equation of state of seawater. *Deep Sea Res.A*, 28(6):625–629.

Mouriño-Carballido, B. and Neuer, S. (2008). Regional Differences in the role of eddy pumping in the North Atlantic subtropical gyre. Historical Conumdrums revisited. *Oceanography*, 21(2):52–61.

Neuer, S., Cianca, A., Helmke, P., Freudenthal, T., Davenport, R., Meggers, H., Knoll, M., Santana-Casiano, J. M., González-Davila, M., Rueda, M.-J., and Llinás, O. (2007). Biogeochemistry and hydrography in the eastern subtropical North Atlantic gyre. Results from the European time-series station ESTOC. *Prog. Oceanogr.*, 72(1):1–29.

22

Neuer, S., Davenport, R., Freudenthal, T., Wefer, G., Llinás, O., Rueda, M.-J., Steinberg, D. K., and Karl, D. M. (2002). Differences in the biological carbon pump at three subtropical ocean sites. *Geophys. Res. Lett.*, 29(18):1885.

Neuer, S., Ratmeyer, V., Davenport, R., Fischer, G., and Wefer, G. (1997). Deep water particle flux in the Canary Island region: seasonal trends in relation to long-term satellite derived pigment data and lateral sources. *Deep Sea Res. I*, 44(8):1451–1466.

Ono, S., Ennyu, A., Najjar, R. G., and Bates, N. R. (2001). Shallow remineralization in the Sargasso Sea estimated from seasonal variations in oxygen, dissolved inorganic carbon and nitrate. *Deep-Sea Res. II*, 48(8-9):1567–1582.

Owens, S. A., Buesseler, K. O., Lamborg, C. H., Valdes, J., Lomas, M. W., Johnson, R. J., Steinberg, D. K., and Siegel, D. A. (2013). A new time series of particle export from neutrally buoyant sediments traps at the Bermuda Atlantic Time-series Study site. *Deep. Res. I*, 72:34–47.

Packard, T. (1971). The measurement of respiratory electron transport activity in marine phytoplankton. *J. mar. Res*, 29:235–244.

Packard, T., Denis, M., Rodier, M., and Garfield, P. (1988). Deep-ocean metabolic CO 2 production: calculations from ETS activity. *Deep Sea Res. Part A.*, 35(3):371–382.

Paulson, C. A. and Simpson, J. J. (1977). Irradiance measurements in the upper ocean. *J. Phys. Oceanogr*, 7(6):952–956.

Pelegrí, J., Arístegui, J., Cana, L., González-Dávila, M., Hernández-Guerra, A., Hernández-León, S., Marrero-Díaz, A., Montero, M. F., Sangrà, P., and Santana-Casiano, M. (2005). Coupling between the open ocean and the coastal upwelling region off northwest Africa: water recirculation and offshore pumping of organic matter. *J. Mar. Syst.*, 54(1-4):3–37.

Putzeys, S., Yebra, L., Almeida, C., Bécognée, P., and Hernández-León, S. (2011). Influence

23

of the late winter bloom on migrant zooplankton metabolism and its implications on export fluxes. *J. Mar. Syst.*, 88(4):553–562.

Reinthaler, T., Van Aken, H., Veth, C., Aristegui, J., Robinson, C., Williams, P., Lebaron, P., and Herndl, G. (2006). Prokaryotic respiration and production in the meso- and bathypelagic realm of the eastern and western North Atlantic basin. *Limnol. Oceanogr.*, 51(3):1262–1273.

Sangrà, P., Pascual, A., Rodríguez-Santana, A., Machín, F., Mason, E., McWilliams, J. C., Pelegrí, J. L., Dong, C., Rubio, A., Arístegui, J., Marrero-Díaz, A., Hernández-Guerra, A., Martínez-Marrero, A., and Auladell, M. (2009). The Canary Eddy Corridor: A major pathway for long-lived eddies in the subtropical North Atlantic. *Deep Sea Res. I*, 56(12):2100–2114.

Schmitt, R. W., Ledwell, J. R., Montgomery, E. T., Polzin, K. L., and Toole, J. M. (2005). Enhanced Diapycnal Mixing by Salt Fingers in the Thermocline of the Tropical Atlantic. *Science*, 308(5722):685–688.

Siegel, D. A. and Deuser, W. G. (1997). Trajectories of sinking particles in the Sargasso Sea: modeling of statistical funnels above deep-ocean sediment traps. *Deep Sea Res. I*, 44(9-10):1519–1541.

Steinberg, D. K., Carlson, C. A., Bates, N. R., Goldthwait, S. A., Madin, L. P., and Michaels, A. F. (2000). Zooplankton vertical migration and the active transport of dissolved organic and inorganic carbon in the Sargasso Sea. *Deep Sea Res. I*, 47(1):137–158.

Weinbauer, M. G., Liu, J., Motegi, C., Maier, C., Pedrotti, M. L., Dai, M., and Gattuso, J. P. (2013). Seasonal variability of microbial respiration and bacterial and archaeal community composition in the upper twilight zone. *Aquat. Microb. Ecol.*, 71(2):99–115.
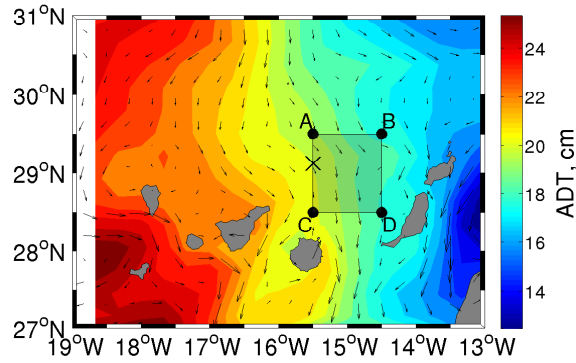
Figure 1: Location of the ESTOC site (×). Letters (A, B, C and D) indicate the four gridpoints from the World Ocean Atlas 2009 and GLODAP databases located closest to ESTOC. Background color is the averaged field of absolute dynamic topography (ADT) for the period 1996-2010 computed from the AVISO dataset. Arrows correspond to geostrophic surface velocities also derived from AVISO.
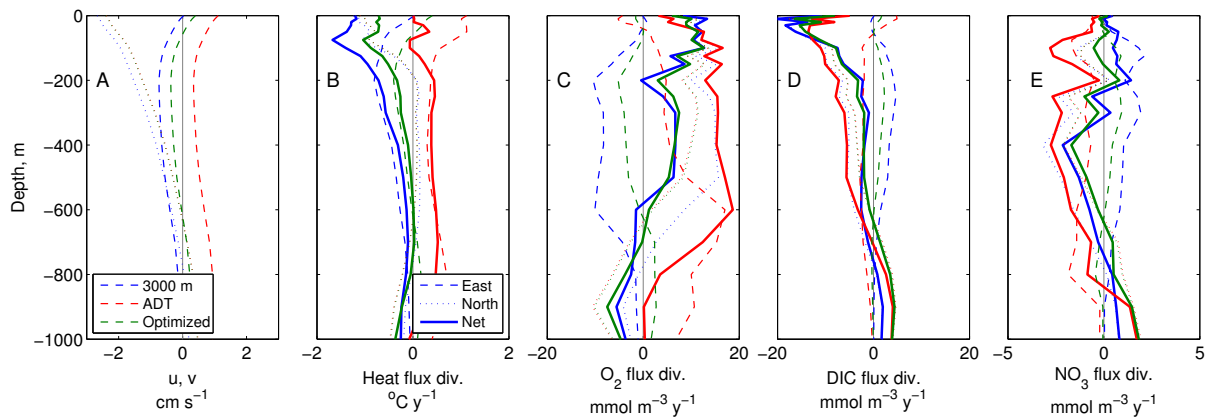

Figure 2: Vertical profiles of (A) geostrophic velocities, geostrophic flux divergence of (B) heat, (C) dissolved oxygen, (D) dissolved inorganic carbon, and (E) nitrate. Three different reference velocities were used for the integration of the thermal wind equations: no-motion level at 3000 m (blue), surface geostrophic velocities computed from the averaged absolute dynamic topography field (ADT) (red), and surface velocities optimized from the temperature model (green). The longitudinal (eastward), latitudinal (northward) and net components are represented by the dashed, dotted, and solid lines, respectively.
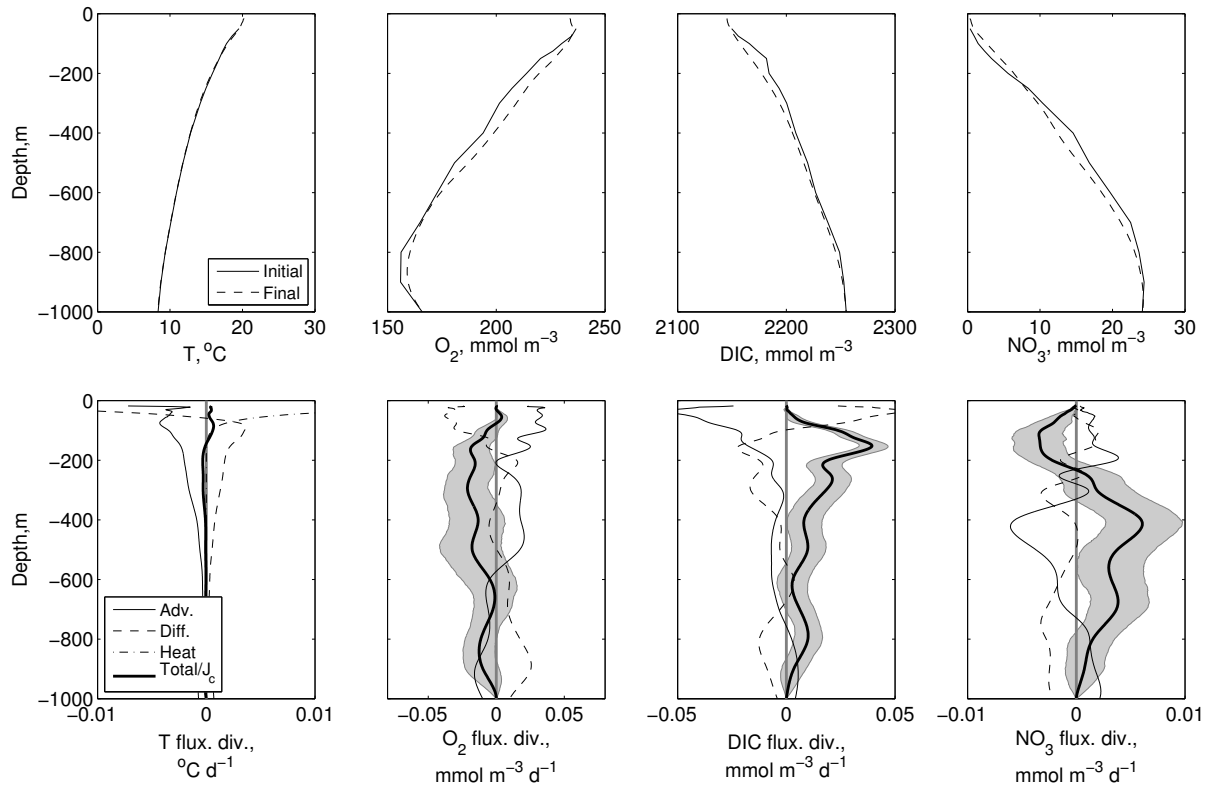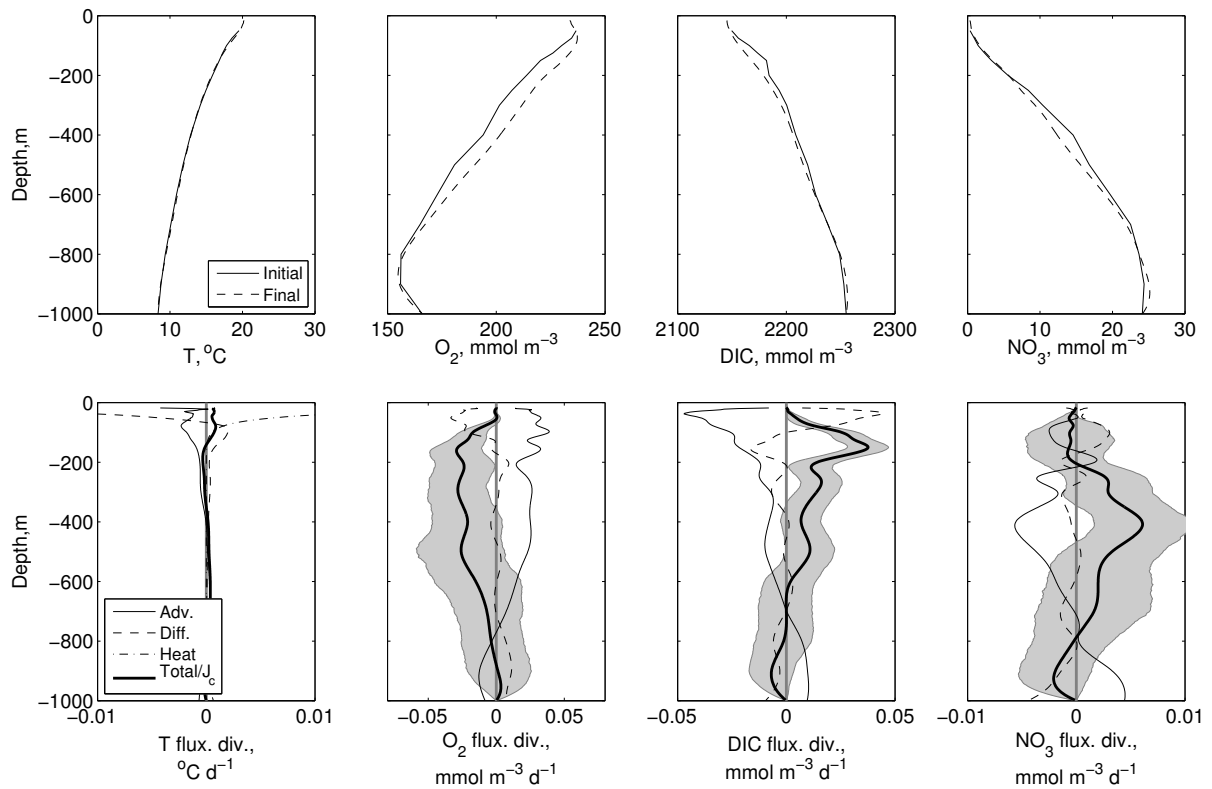
Figure 3: Vertical profiles of model results computed by using as reference the no-motion level at 3000 m. Upper panels correspond to initial (solid line, observed) and final (dashed line, modelled) profiles of temperature (T), oxygen (O_2), dissolved inorganic carbon (DIC) and nitrate (NO_3). Lower panels are total advection flux divergence (Adv., solid line), diffusive flux divergence (Diff., dashed line), solar heating (Heat, dotted–dashed) and the net photosynthesis minus respiration term (J_C, thick black line) for O_2, DIC and NO_3. For temperature the thick black line represents the net (Total) rate of change. The 25% and 75% percentiles of the biological rate diagnosed from the Monte Carlo simulations are delimited by the shaded area.
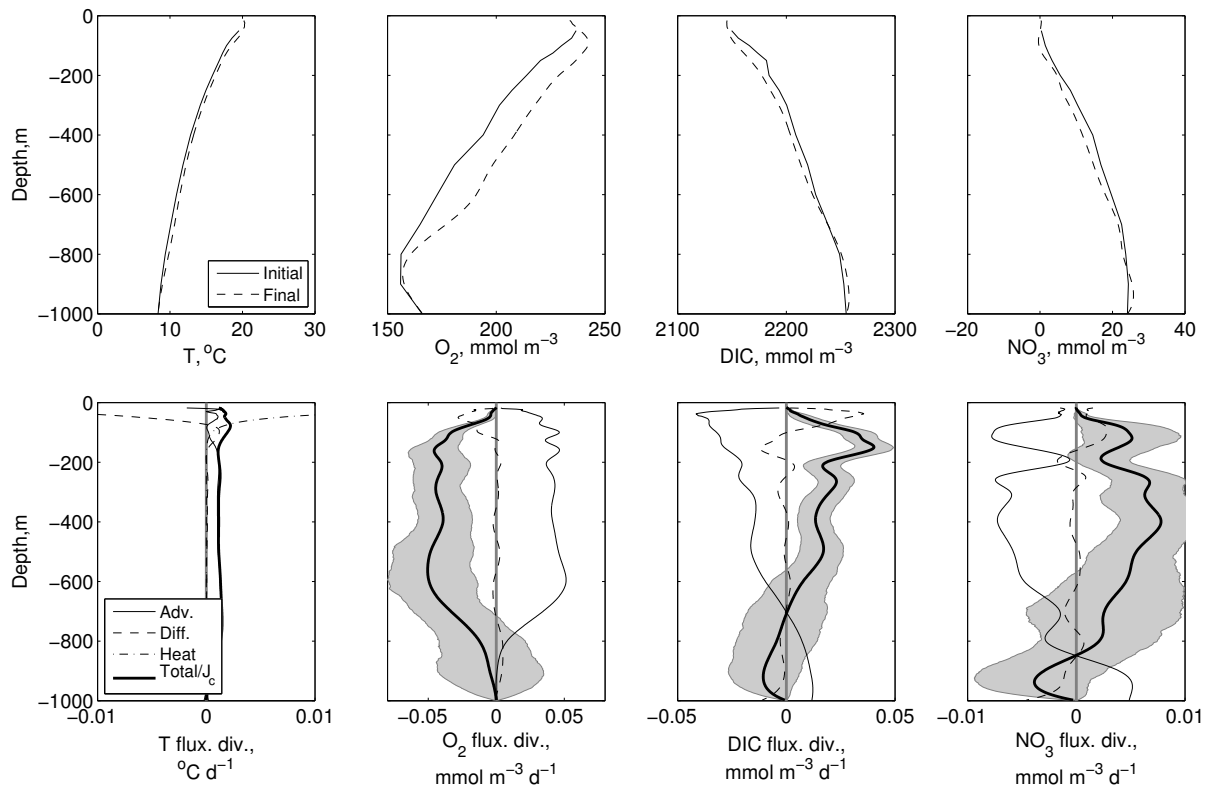
Figure 4: Vertical profiles of model results computed by using reference surface velocities derived from the averaged field of absolute dynamic topography (ADT). Upper panels correspond to initial (solid line, observed) and final (dashed line, modelled) profiles of temperature (T), oxygen (O_2), dissolved inorganic carbon (DIC) and nitrate (NO_3). Lower panels are total advection flux divergence (Adv., solid line), diffusive flux divergence (Diff., dashed line), solar heating (Heat, dotted–dashed) and the net photosynthesis minus respiration term (J_C, thick black line) for O_2, DIC and NO_3. For temperature the thick black line represents the net (Total) rate of change. The 25% and 75% percentiles of the biological rate diagnosed from the Monte Carlo simulations are delimited by the shaded area.
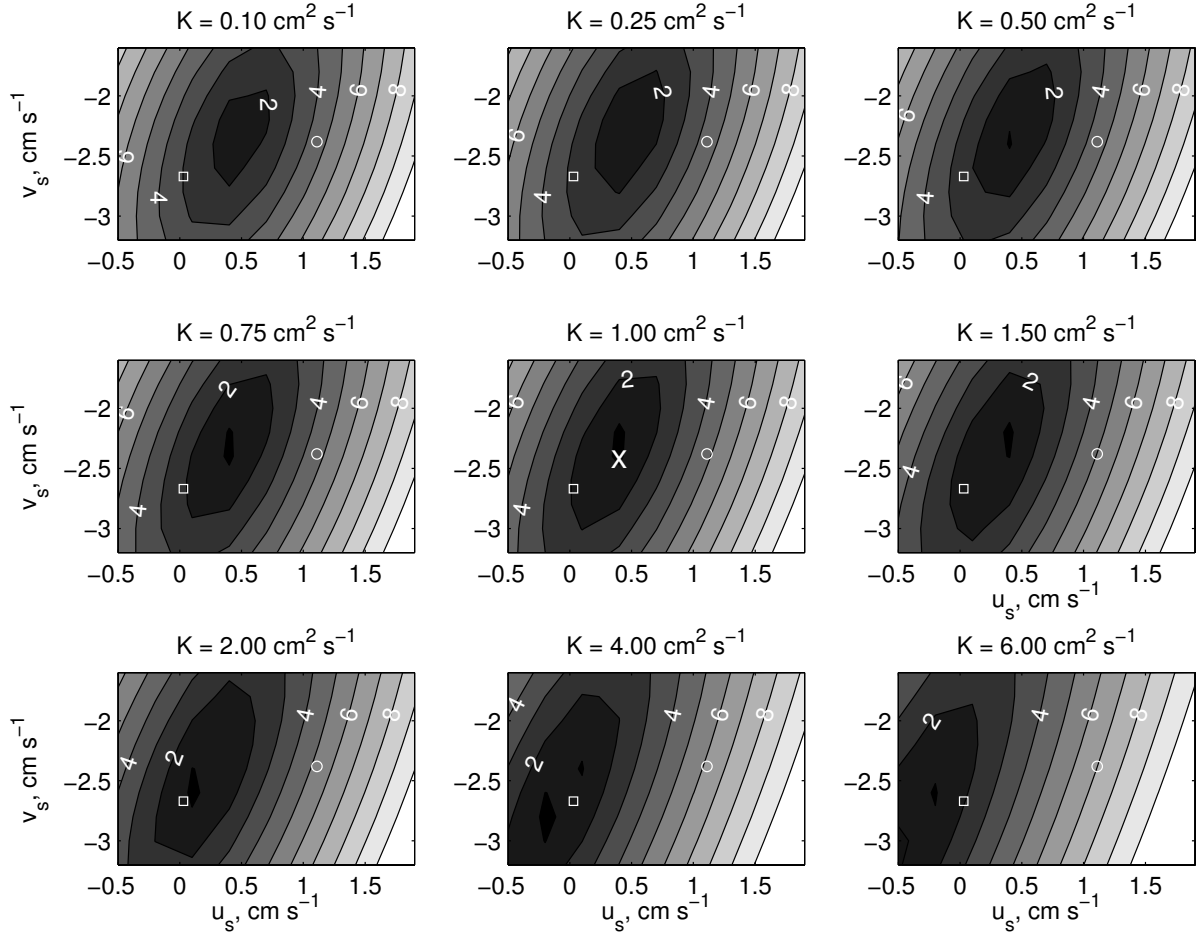
Figure 5: Temperature costs function (%) evaluated for a range of vertical diffusivity (K) and reference surface velocities used for the geostrophic transport calculation (u_s, v_s). The □ and ○ represent the surface geostrophic velocities calculated from the thermal wind equations by using as reference the no-motion level at 3000 m, and the averaged field of absolute dynamic topography (ADT), respectively (see Table 1). The white × indicates the optimal values chosen for K, u_s and v_s. K values higher than $1\,\mathrm{cm^2\,s^{-1}}$ were considered unrealistic.

Figure 6: Vertical profiles of model results computed by using reference surface velocities diagnosed from the temperature model. Upper panels correspond to initial (solid line, observed) and final (dashed line, modelled) profiles of temperature (T), oxygen (O_2), dissolved inorganic carbon (DIC) and nitrate (NO_3). Lower panels are total advection flux divergence (Adv., solid line), diffusive flux divergence (Diff., dashed line), solar heating (Heat, dotted–dashed) and the net photosynthesis minus respiration term (J_C, thick black line) for O_2, DIC and NO_3. For temperature the thick black line represents the net (Total) rate of change. The 25% and 75% percentiles of the biological rate diagnosed from the Monte Carlo simulations are delimited by the shaded area.
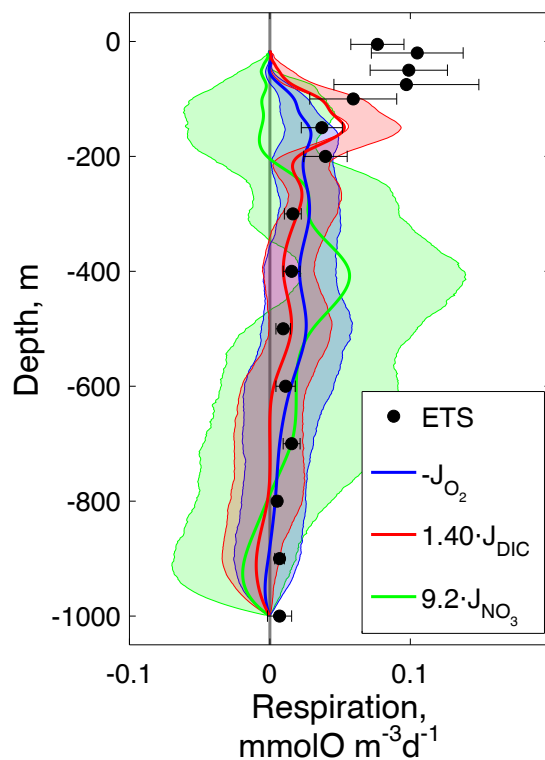
Figure 7: Vertical distribution of averaged respiration rates estimated from the tracer conservation model and from enzymatic electron transport system (ETS) measurements carried out at the ESTOC site. Error bars correspond to standard deviations. Blue, red and green thick lines represent the biological terms for oxygen (O_2), dissolved inorganic carbon (DIC) and nitrate (NO_3) respectively, computed from the tracer conservation model for the optimal K, u_s and v_s configuration. The J_{DIC} term was converted to oxygen units assuming Redfield stoichiometry. The 25% and 75% percentiles of the biological terms diagnosed from the Monte Carlo simulations are delimited by the shaded areas.
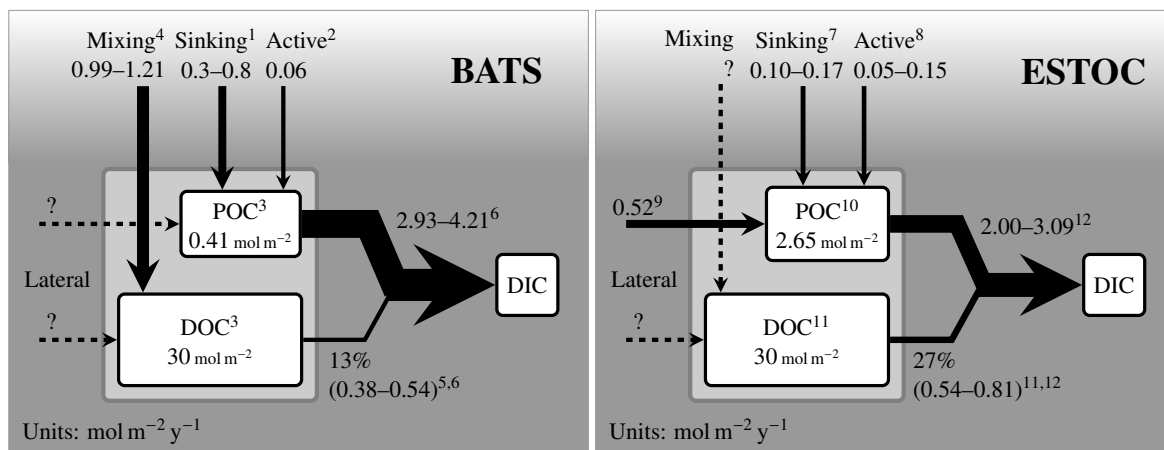
Figure 8: Mesopelagic carbon budget for the BATS (Bermuda Atlantic Time-Series Study, 31.7°N-64.2°W) and ESTOC (European Station for Time-Series in the Ocean, 15.5 °W, 29.1 °N) sites. Units are mol m^{-2} y^{-1} unless indicated; DIC, dissolved inorganic carbon, POC and DOC, particulate and dissolved organic carbon, respectively. References: [1]Helmke et al. (2010), Owens et al. (2013); [2]Steinberg et al. (2000); [3]http://bats.bios.edu/; [4]Carlson et al. (1994);[5] Emerson (2014); [6]Jenkins and Goldman (1985); [7]Helmke et al. (2010); [8]Putzeys et al. (2011); [9]Alonso-González et al. (2009); [10]Neuer et al. (2007); [11]Arístegui et al. (2003b); [12] this study.
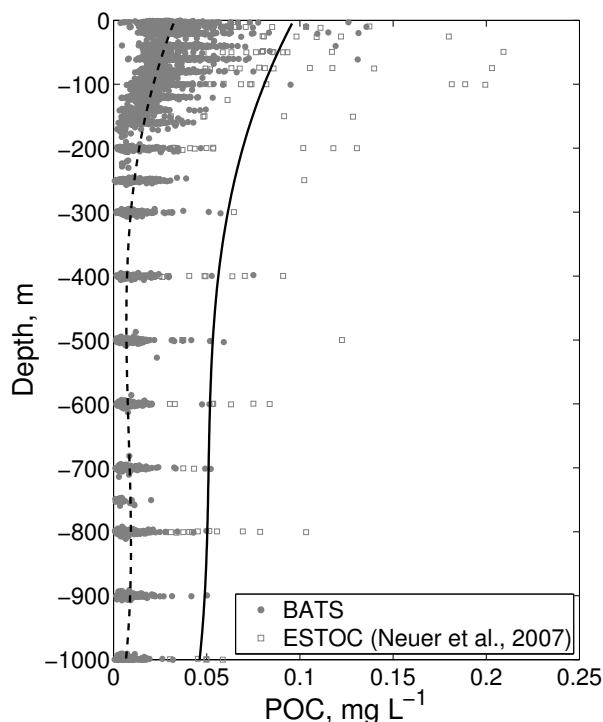
Figure 9: Vertical distribution of particulate organic carbon (POC) for the BATS and ESTOC sites. Data for BATS correspond to the 1988-2012 period (http://bats.bios.edu/), whereas for ESTOC were adapted from Neuer et al. (2007) and correspond to the 1996-1999 period. Polynomial (cubic) fits are shown.

Table 1: Geostrophic transports computed by using three different reference velocities: no-motion level at 3000 m, surface geostrophic velocities computed from the averaged field of absolute dynamic topography (ADT), and optimal surface velocities diagnosed from the temperature model. u_s and v_s are the eastward and northward surface velocities, respectively. Depth-integrated (150–700 m) longitudinal, latitudinal and net geostrophic flux divergences are shown for temperature (T), oxygen (O_2), dissolved inorganic carbon (DIC) and nitrate (NO_3).

		Geostrophic velocity reference		
		3000 m	ADT	Optimized
u_s, cm s^{-1}		0.03 ± 0.52	1.11 ± 0.66	0.40 ± 0.20
v_s, cm s^{-1}		-2.67 ± 0.37	-2.39 ± 0.78	-2.40 ± 0.20
T	Long. Flux. Div.	-259 ± 49	209 ± 56	-98 ± 43
	Lat. Flux. Div.	56 ± 44	24 ± 37	25 ± 37
°C m y^{-1}	Net Flux. Div.	-203 ± 66	233 ± 67	-73 ± 57
O_2	Long. Flux. Div.	-4.78 ± 2.08	4.80 ± 2.31	-1.50 ± 1.08
	Lat. Flux. Div.	6.75 ± 2.39	3.91 ± 1.60	4.06 ± 1.63
mol m^{-2} y^{-1}	Net Flux. Div.	1.97 ± 3.17	8.71 ± 2.81	2.56 ± 1.96
DIC	Long. Flux. Div.	1.65 ± 0.79	-1.28 ± 1.04	0.65 ± 0.38
	Lat. Flux. Div.	-2.87 ± 0.92	-1.64 ± 0.62	-1.70 ± 0.64
mol m^{-2} y^{-1}	Net Flux. Div.	-1.22 ± 1.21	-2.92 ± 1.22	-1.06 ± 0.74
NO_3	Long. Flux. Div.	0.63 ± 0.34	-0.54 ± 0.43	0.23 ± 0.16
	Lat. Flux. Div.	-0.98 ± 0.38	-0.50 ± 0.25	-0.53 ± 0.25
mol m^{-2} y^{-1}	Net Flux. Div.	-0.35 ± 0.52	-1.04 ± 0.49	-0.30 ± 0.30

Table 2: Depth-integrated (150–700 m) model terms computed from the model runs using three different reference levels: no-motion level at 3000 m, surface geostrophic velocities computed from the averaged field of absolute dynamic topography (ADT), and optimal surface velocities diagnosed from the temperature model. Optimal diffusivity (K_{op}), horizontal advection (H. adv), vertical advection (V. adv), vertical diffusion (V. diff.), solar heating and biological remineralization (Remin.) terms are shown. The model cost for the temperature model and the detection limit for the respiration rates are also shown (see Methods).

		Geostrophic velocity reference		
		3000 m	ADT	Optimized
K_{op} cm^2 s^{-1}		3.9	0.4	1.0
T	H. adv	-237 ± 206	198 ± 183	-52 ± 299
	V. adv	31 ± 119	31 ± 121	31 ± 119
°C m y^{-1}	V. diff.	179 ± 115	15 ± 20	42 ± 32
	Solar Heat	0.37 ± 0.01	0.37 ± 0.01	0.37 ± 0.01
	Cost	1.8%	3.0%	1.6%
O_2	H. adv	1.56 ± 4.56	8.42 ± 4.30	3.80 ± 7.41
	V. adv	0.41 ± 1.59	0.42 ± 1.62	0.41 ± 1.60
mol m^{-2} y^{-1}	V. diff.	0.75 ± 0.84	0.02 ± 0.26	0.18 ± 0.45
	Remin.	-2.72 ± 3.90	-8.86 ± 3.93	-4.39 ± 7.02
	Det.Lim.	0.38	0.61	0.35
DIC	H. adv	-5.08 ± 15.50	-6.86 ± 15.54	-5.56 ± 15.68
	V. adv	3.89 ± 15.34	3.89 ± 15.35	3.89 ± 15.35
mol m^{-2} y^{-1}	V. diff.	-1.27 ± 0.78	-0.12 ± 0.13	-0.33 ± 0.21
	Remin.	2.46 ± 1.62	3.09 ± 1.63	2.00 ± 2.63
	Det.Lim.	0.43	1.01	0.40
NO_3	H. adv	-0.35 ± 0.69	-1.03 ± 0.70	-0.50 ± 1.07
	V. adv	0.01 ± 0.03	0.00 ± 0.02	0.01 ± 0.03
mol m^{-2} y^{-1}	V. diff.	-0.20 ± 0.18	-0.04 ± 0.06	-0.07 ± 0.09
	Remin.	0.54 ± 0.64	1.07 ± 0.68	0.57 ± 1.05
	Det.Lim.	0.09	0.22	0.08